The effects of tertiary dendrite arm spacing and segregation on the corrosion behavior of a Pb–Sb alloy for lead-acid battery components

Wislei R. Osório [a,b,*], Emmanuelle S. Freitas [b], Leandro C. Peixoto [b], José E. Spinelli [c], Amauri Garcia [b]

[a] School of Applied Sciences – FCA, University of Campinas – UNICAMP, Campus Limeira, 1300, Pedro Zaccaria St., Jd. Sta Luiza, 13484-350 Limeira, SP, Brazil
[b] Department of Materials Engineering, University of Campinas – UNICAMP, PO Box 6122, 13083-970 Campinas, SP, Brazil
[c] Department of Materials Engineering, Federal University of São Carlos – UFSCar, 13565-905 São Carlos, SP, Brazil

ABSTRACT

The aim of this study is to evaluate the effects of segregation and of the presence of tertiary dendrite arms in the microstructural arrangement of a Pb–Sb alloy on its resultant corrosion behavior. In this context, a water-cooled unidirectional solidification system was used to obtain alloy samples having different dendritic patterns. Electrochemical impedance spectroscopy and potentiodynamic polarization curves were used to analyze the corrosion resistance in a 0.5 M H_2SO_4 solution at 25 °C. Three different dendritic arrays were investigated as a function of the cooling rate and antimony macrosegregation profile. It was found that the tertiary dendritic arms associated with the antimony segregation have an important role on the resulting corrosion response. It is shown that the sample with a well defined tertiary dendritic array provide a more homogeneously distributed interdendritic eutectic mixture exhibiting better corrosion protection.

© 2012 Elsevier B.V. All rights reserved.

1. Introduction

It is well-known that Pb–Sb alloys are commonly used in the production of positive and negative grids, connectors and other components of both VRLA-valve-regulated lead acid and SLI-starting, lighting and ignition batteries [1–3]. There exists a number of manufacturing process generally used to produce these aforementioned components which generates different resulting microstructures [1,2]. It is also known that the antimony content of a Pb–Sb electrode affects the mechanical properties, the microstructure, the electrochemical behavior of active materials and corrosion layers on the electrode [1–6].

The cellular and dendritic arm spacings are important microstructural parameters affecting the segregation and mechanical properties. In particular the scale of cellular and secondary dendritic spacings was shown to strongly influence the overall surface corrosion resistance of binary lead-base alloys [7–15].

In a recent article, it was shown that coarser cellular structures tend to yield higher corrosion resistance than finer cellular structures for a dilute Pb–0.85 wt.% Sb alloy [7]. Such tendency was associated with the reduction of cellular boundaries when compared with finer cells, since the boundary has proved to be more susceptible to corrosion. It is known that antimony, which is segregated toward the cell boundaries and interdendritic regions during solidification of Pb–Sb alloys, has an important role on the corrosion behavior [7,8]. It was also concluded that finer dendritic arrays of Pb–Sb alloys tend to yield higher corrosion resistances than coarser dendritic structures [7]. The dendritic array morphology has the antimony-rich regions located in the lamellar eutectic mixture. The Sb-rich lamellae will envelope the Pb-rich phase more efficiently when the microstructure is characterized by finer dendritic spacings, due to the more extensive distribution of the eutectic mixture, and thus contributing to the protection of the Pb-rich matrix against the corrosion action [7]. Previous studies [7–15] evidenced that coarse cellular samples were associated with better corrosion resistance than fine cellular samples when considering experimental studies with Pb-based alloys subjected to corrosion tests in a sulfuric acid (H_2SO_4) solution. In another recent article [13], it was found that the experimental current density increased with the increase in both the Sb content and dendritic spacing, when the dendritic morphological arrays of Pb–2.2 and 6.6 wt.% Sb alloys were compared. It was concluded that independently of the micromorphological array, the Pb–2.2 wt.% Sb alloy sample has better corrosion resistance than both Pb–1 and 6.6 wt.% Sb alloys [13].

Mechanical strength and ductility are influenced by the dimensions and continuity of the primary dendritic branches. Campbell [16] stated that dendrite arm spacing (DAS) usually refers to the spacing between the secondary arms of dendrites. However, if tertiary arms were present at a smaller spacing, then it would refer

* Corresponding author at: School of Applied Sciences – FCA, University of Campinas – UNICAMP, 13484-350, Campus Limeira, Limeira, SP, Brazil.
Tel.: +55 19 3701 6676; fax: +55 19 3776 6711.
E-mail address: wislei.osorio@fca.unicamp.br (W.R. Osório).

to this. The availability of studies on tertiary dendrite arms is very restricted. As mentioned, in Pb–Sb components smaller DAS yield higher corrosion resistance than coarser dendritic structures. In this context, tertiary dendrite arms may contribute with a more homogeneous distribution of the anodic Pb-rich phase.

The aim of this study was to examine the effect of the presence of tertiary dendrite arms on the microstructural arrangement of Pb–Sb alloys on the resultant electrochemical corrosion behavior. For this purpose, a Pb–3.5 wt.% Sb alloy and a water cooled unidirectional solidification system were used were used to provide different dendrite patterns. Corrosion tests were performed with samples of different dendrite arm spacings in a 0.5 M H_2SO_4 solution at 25 °C, and the corrosion rate was correlated with both the resulting microstructure and the Sb segregation profile along the casting length.

2. Experimental procedure

A Pb–3.5 wt.% Sb alloy was prepared from commercially pure (c.p.) metals: Pb (99.97 wt.%) and Sb (99.99 wt.%). The mean impurities detected were: Fe (0.12 wt.%), Si (0.05 wt.%), Cu (0.015 wt.%), besides other elements with concentration less than 50 ppm.

A water-cooled unidirectional solidification system was used in the experiments. The solidification set-up was designed in such way that heat was extracted only through the water-cooled bottom, promoting vertical upward directional solidification, as shown in Fig. 1. The temperatures were monitored during solidification using a bank of type J thermocouples accurately located along the casting length at six different positions with respect to the metal/mold interface: 4, 12, 22, 38, 54 and 68 mm, at the center of the casting. The stainless steel mold had an internal diameter of 50 mm, a height of 110 mm and a wall thickness of 3 mm. The side walls were covered with a layer of insulating alumina to minimize radial heat losses. The bottom part of the mold was closed with a thin (3 mm thick) stainless steel sheet, which physically separates the metal from the cooling fluid.

The cylindrical casting was sectioned on its midplane, ground, polished and etched with a solution to reveal the macrostructure. Transverse sections (perpendicular to the growth direction) extracted from the directionally solidified casting at 6 different positions along its length were polished and etched with a solution (37.5 mL of glacial acetic acid and 15 mL of H_2O_2, at 25 °C) for microscopy. Image processing systems Neophot 32 (Carl Zeiss, Esslingen, Germany) and Leica Quantimet 500 MC (Leica Imaging Systems Ltd, Cambridge, England) were used to measure the dendrite spacings. The λ_3 values were measured on the transverse section by averaging the distance between adjacent side branches. These measurements, about 20 values for each selected position from the metal/mold interface, were confirmed by comparison with values measured on longitudinal sections. The macrosegregation profile was determined by a scanning electron microscope (SEM, JMS T20 of Jeol Co., Japan) and an energy dispersive X-ray analyzer (EDAX, NORAN, System Six 1.5, USA).

In order to establish correlations between the corrosion resistance and the microstructural pattern, electrochemical impedance spectroscopy (EIS) and polarization tests were carried-out on samples collected at different positions along the casting length. The EIS tests were carried-out in a 500 cm^3 of sulfuric acid solution (0.5 mol L^{-1}) at 25 °C. Electrochemical corrosion tests were performed in a 1 cm^2 circular area of ground (600 and 1200 grit SiC finish) alloy samples. Electrochemical impedance spectroscopy (EIS) measurements began after an initial delay of 15 min for the samples to reach a steady-state condition. These tests were carried out in a stagnant and naturally aerated 500 cm^3 of a 0.5 M H_2SO_4 solution at 25 °C under a pH of about 0.86 (±0.14), used

to simulate the battery electrolytic fluid. A potentiostat (EG & G Princeton Applied Research, model 273A) coupled to a frequency analyzer system (Solartron model 1250), a glass corrosion cell kit with a platinum counter-electrode and a saturated calomel reference electrode (SCE) were used to perform the EIS tests. The potential amplitude was set to 10 mV at open-circuit, peak-to-peak (AC signal), with 5 points per decade and the frequency range was set from 100 mHz to 100 kHz. Although the SCE electrode is not commonly used in lead-acid system studies, a SCE electrode can also be used as a reference electrode since the one inconvenient is the fact that chloride may contaminate the electrolyte, and other is to convert from SCE to MSE or other potential scales (ASTM G3).

Potentiodynamic measurements were also carried out in the aforementioned solution at 25 °C using a potentiostat at the same positions where the EIS tests were carried out. These tests were conducted by stepping the potential at a scan rate of 0.1667 mV s^{-1} from −0.75 V (SCE) to −0.35 V (SCE) at open-circuit. Using an automatic data acquisition system, the potentiodynamic polarization curves were plotted and both corrosion rate and potential were estimated by Tafel plots by using both anodic and cathodic branches at a scan rate of 0.1667 mV s^{-1} from −250 mV (SCE) to +250 mV (SCE) at open-circuit. This mentioned potentiodynamic range corresponds with −600 mV to −150 mV vs. MSE–Mercury/Mercurous Sulfate Electrode or Hg/Hg_2SO_4 electrode [17]. Duplicate tests for EIS and potentiodynamic polarization curves were carried out. In order to supply quantitative support for discussions of these experimental EIS results, an appropriate model (ZView version 2.1b) for equivalent circuit quantification has also been used.

3. Results and discussion

3.1. Macrostructure, microstructure and cooling rate

The macrostructure of the resulting directionally solidified Pb–3.5 wt.% Sb alloy casting is shown in Fig. 2(a). Columnar grains prevailed along the entire casting length, as previously obtained in other similar experiments using Pb-based alloys [7–15]. The positions in the casting from where the samples for microstructure characterization and corrosion tests were extracted are also indicated in Fig. 2(a). The following distances from the bottom of the casting (casting surface) were examined: P1 (8 mm), P2 (25 mm) and P3 (50 mm). Fig. 2(b) evidences the experimental results of the tip cooling rate during solidification as a function of position (distance) from the cooled bottom of the casting. It can be seen that the cooling rate is high for initial positions and that it decreases with the increase in distance from the bottom of the casting. The experimental Sb macrosegregation profile along the casting length is shown in Fig. 2(c).

The experimental evolution of the dendrite arm spacings (both primary, λ_1, and tertiary, λ_3) as a function of the resulting cooling rate is shown in Fig. 3. Points are experimental results and the line represents an empirical power function fit to the experimental points. Minimum and maximum measured dendrite spacings for each position are expressed by the error bars. As expected, the use of a water-cooled mould imposed higher values of tip cooling rates near the casting/chill surface and a decreasing profile along the casting length. This is correlated with the increase in the thermal resistance of the solidified shell with distance from the cooled surface. As a result, the dendritic array is fine close to the casting cooled surface and coarse far from it.

It is also interesting to observe in Fig. 3(a) that the experimental range of cooling rates varied from 6 to about 0.06 K s^{-1}, but the initial growth of tertiary dendrite arms was found to occur only for cooling rates lower than 0.4 K s^{-1}. It can be seen that the tertiary dendrite spacing is about 3.7 times lower than the primary dendrite
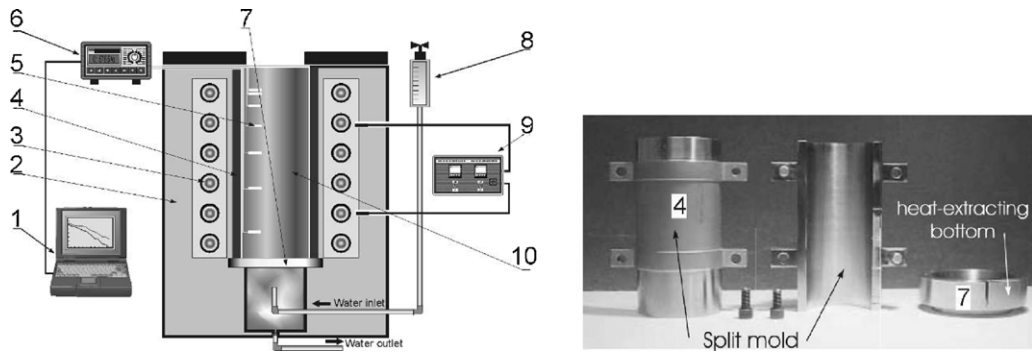
Fig. 1. Schematic representation of the experimental solidification set-up: (1) computer and data acquisition software; (2) insulating ceramic shielding; (3) electric heaters; (4) mold; (5) thermocouples; (6) data logger; (7) heat-extracting bottom; (8) water flow meter; (9) temperature controller; and (10) casting.

spacing for the range of cooling rates experimentally examined. A λ_1/λ_3 ratio of about 5 has been reported for Al–Cu alloys unidirectionally solidified [18]. It has also been reported that the tertiary array has a growth character which is very similar to that of cells and primary dendrite arms [18]. The influence of typical solute normal macrosegregation on the tertiary spacings can be examined by comparing the relative position of the average experimental points as a function of position along the casting length, as shown in Fig. 2(c).

It seems that the Sb content associated with the local solidification cooling rate affect the development of dendritic tertiary arms. Higher cooling rates associated with lower Sb content (lower than

3.5 wt.% Sb) which are typical of initial positions in the casting (up to 25 mm from the bottom of the casting) provide a microstructural dendritic array which is characterized by primary and secondary dendrite arms. However, for positions where the Sb content is close to or slightly higher than the nominal composition, the presence of tertiary dendritic arms can be detected. Similar normal macrosegregation profiles have also been reported for both dilute Pb–0.85 wt.% Sb and concentrated Pb–6.6 wt.% Sb alloys [7].

The typical microstructures observed on transverse sections of the Pb–3.5 wt.% Sb alloy casting are also shown in Fig. 3. The as-cast microstructure consists of a dendritic Pb-rich matrix (α-phase: solid solution of Sb in Pb) with a lamellar eutectic mixture in the
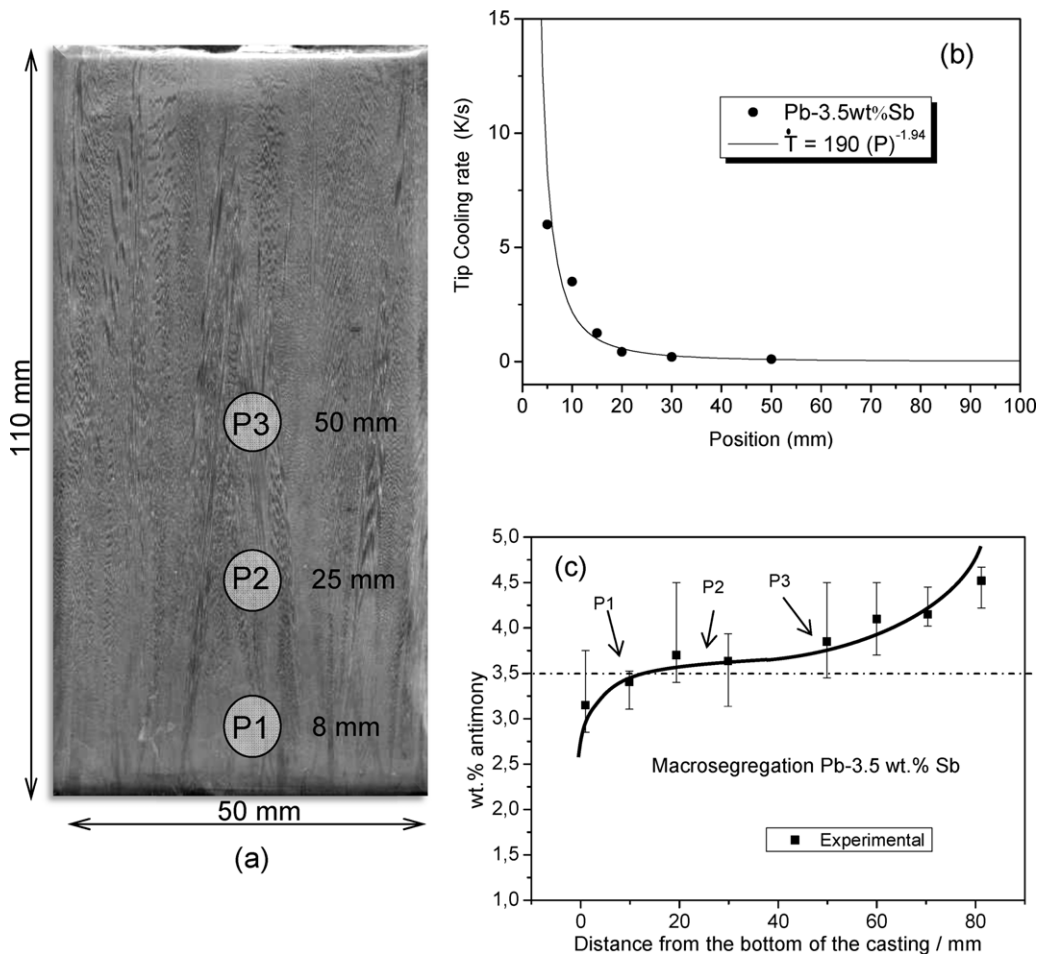

Fig. 2. (a) Macrostructure of a Pb–3.5 wt.% Sb alloy casting; P1, P2 and P3 are the positions in casting from where the samples for microstructure characterization and corrosion tests were extracted, (b) experimental cooling rate during solidification along the casting length, and (c) macrosegregation profile along the casting length.
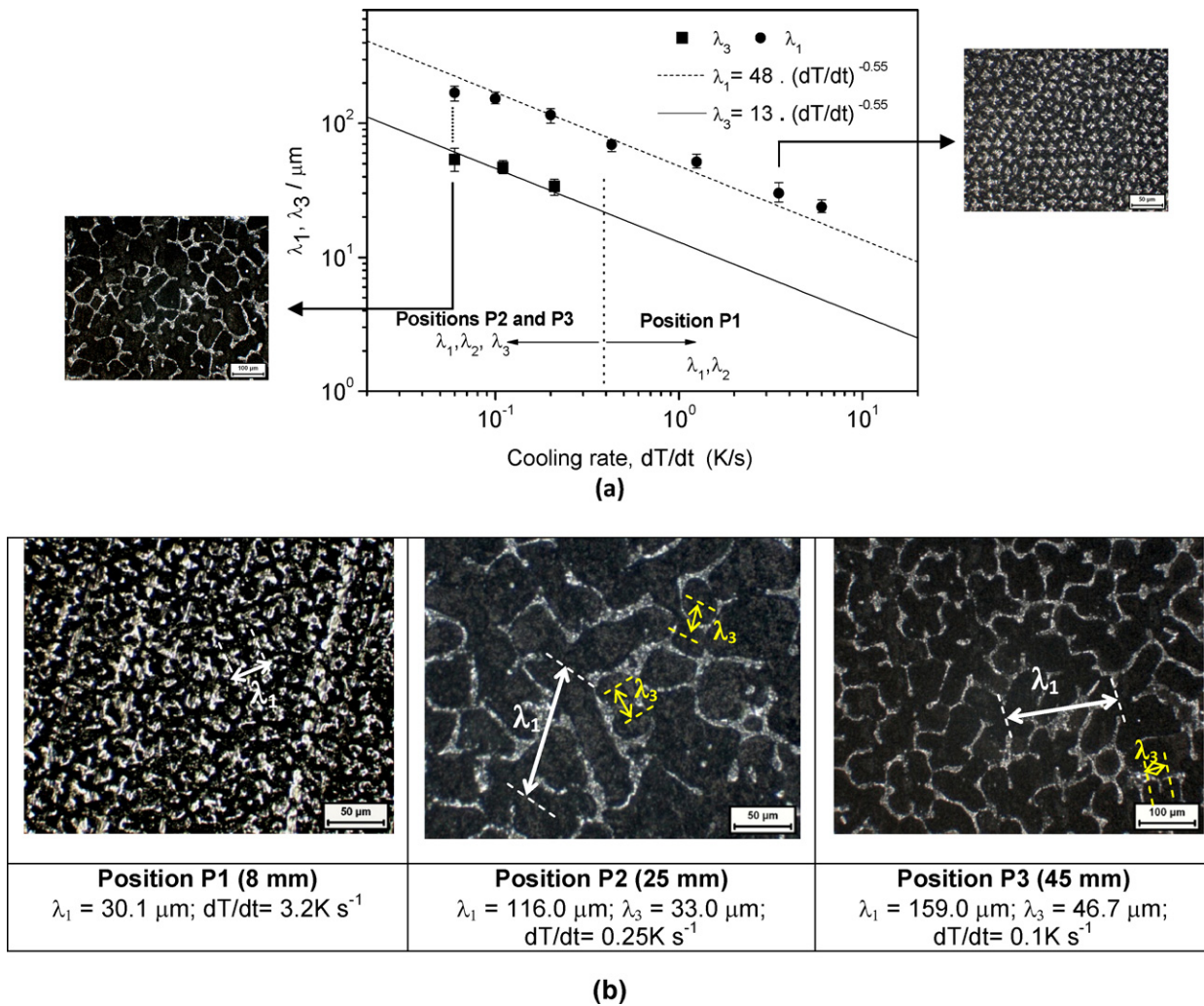
Fig. 3. (a) Evolution of primary and tertiary dendritic arm spacings with the cooling rate. (b) Typical transverse microstructures along the Pb–3.5wt.% Sb alloy casting length.

interdendritic regions constituted of α, and a Sb-rich β-phase (solid solution of Pb in Sb).

3.2. EIS measurements and equivalent circuit

3.2.1. Bode and Bode-phase diagrams

Fig. 4 depicts the Bode, Bode-phase and Nyquist plots representing the modulus of impedance and phase angle as a function of frequency and $Z_{Imaginary}$ and Z_{Real}, respectively.

It seems that two time constants are associated with the corrosion kinetics of the Pb–3.5 wt.% Sb alloy samples when the Bode-phase plots are considered. In a frequency range from 10^4 to 10^5 Hz, a first time constant can be related to the reaction between the electrolyte and the Sb-rich phase in the interdendritic region, which is mainly observed for the sample corresponding to the position P3. This can be associated with the slightly higher Sb content, due to the segregation phenomenon, when compared with the other positions examined along the casting length, as can be observed in Fig. 2(c). In Fig. 4(b), the double layer formation, for frequencies between 10^0 and 10^3 Hz, corresponding to the position P3, is relatively different from those observed for the two other alloy samples, and could be also associated with the Sb segregation profile. In Bode-phase plots, for frequencies from 10^2 to 10^0 Hz, the second time constant correlates with the Pb-rich matrix which

is clearly evidenced for all the samples examined, as depicted in Fig. 4(a).

Considering the Bode-phase plots, the experimental maximum phase angles ($\theta_{max.}$) are about 50, 60 and 47° for frequencies of 90, 50 and 15 Hz at positions P1, P2 and P3, respectively. On the other hand, considering the Bode diagrams, the maximum modulus of impedance ($|Z|$) is attained at a low frequency. Thus, at a frequency of 0.1 Hz, the dendritic arrays at positions P1, P2 and P3 have experimental $|Z|$ values of about 300, 400 and 650 Ω cm^2, respectively. These experimental impedance parameters provide indications that the sample corresponding to the position P3 seems to be correlated with the best electrochemical behavior when compared to the other samples examined. It seems that the tertiary dendritic arm spacing (λ_3) has an important effect on the resulting corrosion resistance. At position P2 the tertiary arms initiate their development from the secondary branches differently of position P1 where the microstructure has no tertiary dendrite arms, as shown in Fig. 3. Besides, it can also be observed a slightly higher Sb content at P2 (Fig. 2) when compared with P1. When comparing the resulting microstructural arrays of positions P3 and P2, it can be seen that the sample of position P3 has tertiary spacings (of about 50 μm) which are coarser than those observed at P2 (λ_3 of about 25 μm) but the continuity of the tertiary arms along the interdendritic region permits the eutectic mixture to be more homogeneously distributed. A schematic representation of primary
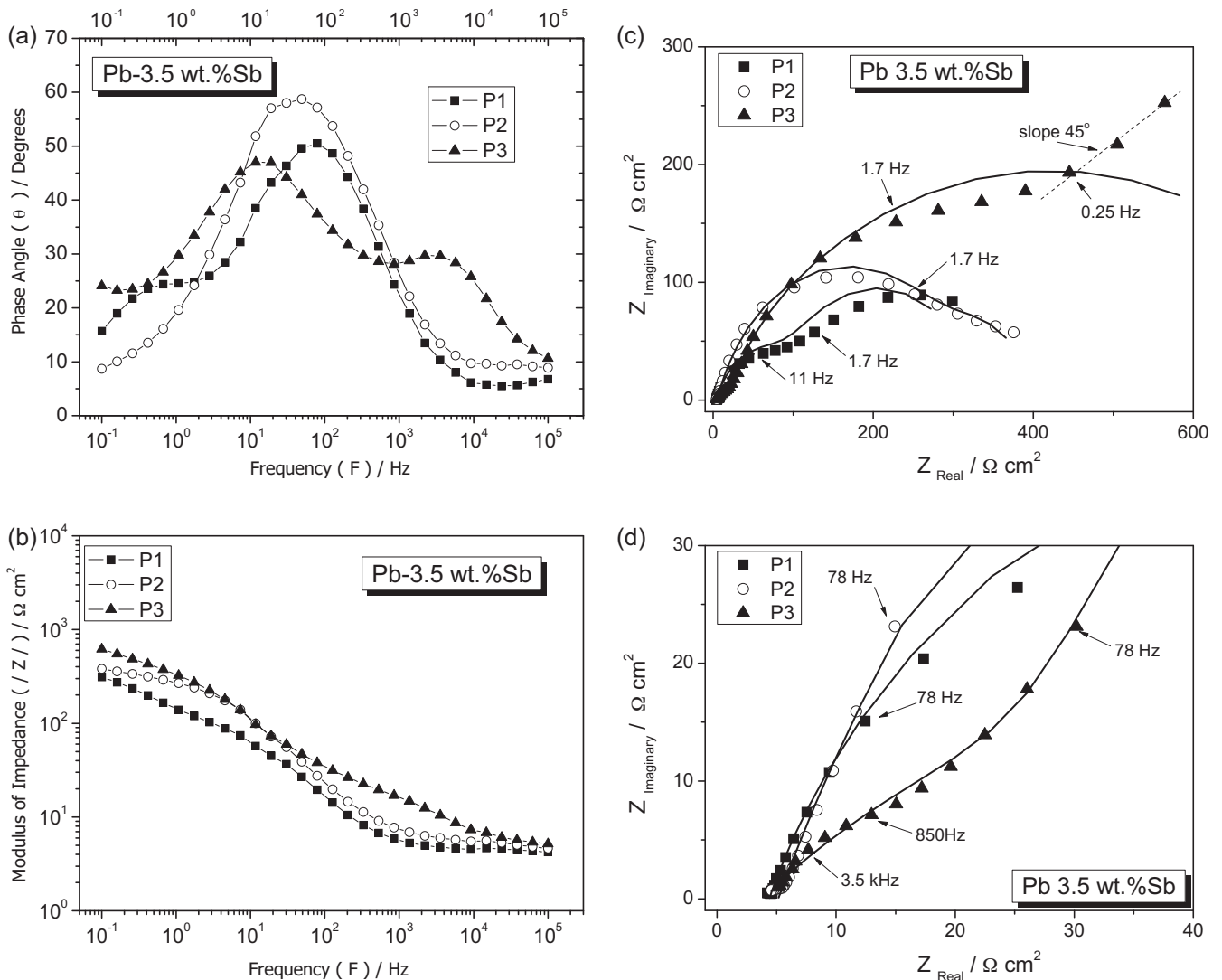
Fig. 4. Experimental data for the Pb 3.5 wt.% Sb alloy samples in a 0.5 M H_2SO_4 solution at 25 °C: (a) Bode-phase, (b) Bode, (c) experimental and simulated Nyquist results and (d) the corresponding details for frequencies lower than 78 Hz.

(λ_1) and tertiary (λ_3) arms in the microstructural dendritic arrays at positions P1, P2 and P3 are shown in Fig. 5. It can be observed that both λ_1 and λ_3 increased with the increase in distance from the bottom of the casting.

Fig. 4(c) and (d) shows simulated and experimental results in Nyquist plots of all examined Pb–3.5 wt.% Sb alloy samples. All Nyquist plots are characterized by a capacitive arc at high frequencies (between 10^5 Hz and 2 Hz), as also previously observed for both Pb–Sb and Pb–Sn as-cast alloys [7–15]. It can also be seen that the Nyquist plot corresponding to the position P3 has a diameter of the capacitive arc which is higher than those corresponding to the samples of the two other positions examined (i.e. P2 and P1). It can also be observed that the Nyquist plot for P3 is the only characterized by a capacitive arc followed by a trend to a slope of about 45° from 0.25 to 0.01 Hz, which can indicate that an oxide film has formed and is thus contributing to better electrochemical behavior.

Another interesting observation is related to the different shape of the Nyquist plot for position P3 at higher frequencies (e.g. 850–3500 Hz). In this range of frequencies, reactions between the work electrode (sample-P3) and the electrolyte are evidenced in the Nyquist plot. This indicates that the sample P3 has a different initial reaction with the sulfuric acid solution. It can be speculated that this difference occurred due to the slightly higher Sb content (up

to 4.5 wt.%) in this sample when compared with those of the other two samples, as shown in Fig. 2(c). This reaction is not the predominant factor connected to the resulting electrochemical corrosion response of sample P3, however, it can give a significant contribution to this when associated with those reactions occurring at low frequencies.

3.2.2. Equivalent circuit and Nyquist diagrams

In order to provide quantitative support to the experimental EIS results, an equivalent circuit analysis has also been performed, as similarly reported in previous studies [7–15,19–23]. Fig. 6 shows the proposed equivalent circuit used to fit the experimental data. The impedance parameters obtained by the ZView® software, are shown in Table 1. The fitting quality was evaluated by chi-squared (χ^2) [8–13] values of about 33×10^{-4} to 98×10^{-4}, as shown in Table 1.

The interpretation of the physical elements of the proposed equivalent circuit is similar to those previously reported [7–15,19–23]. In this sense, the parameters R_{el}, R_1 and R_2 are the electrolyte resistance, the charge transfer resistance and stands for a polarization resistance due to the participation of adsorbed intermediates, respectively. A constant-phase element representing a shift from an ideal capacitor was used instead of the capacitance
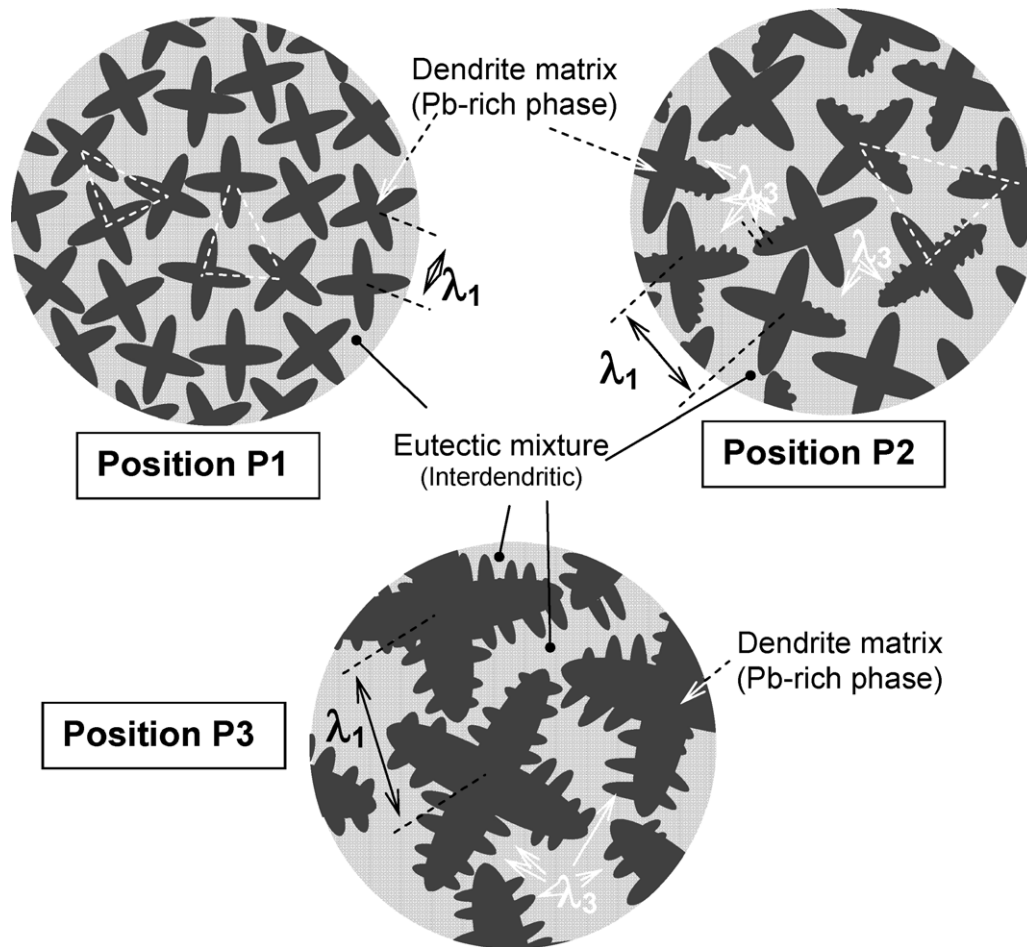
Fig. 5. Schematic representation evidencing primary and tertiary dendrite arms formation for Pb–3.5 wt.% Sb alloy samples at positions P1, P2 and P3.

itself, for simplicity. The parameters $Z_{CPE(1)}$ and $Z_{CPE(2)}$ denote the double layer capacitance and the capacitance associated with the polarization resistance R_2. Values of n_1 and n_2 are correlated with the phase angle, varying between −1 and 1. $Z_{CPE} = [C(j\omega)^n]^{-1}$ denotes the impedance of a constant phase element [7–15,19–23] where C is the capacitance; j is the current; ω is the frequency and $-1 \leq n \leq 1$. The value of n can also be associated with the non-uniform distribution of current as a result of surface defects or roughness [22].

Analyzing the impedance parameters depicted in Table 1, it can be seen that $Z_{CPE(2)}$ is always lower than $Z_{CPE(1)}$. Low capacitances can be associated with both an increase in the passive layer thickness [21] and a decrease in the oxide film dielectric constant which is caused due to variation in the ratio between electrolytic volume and oxide film [21,22,24,25].
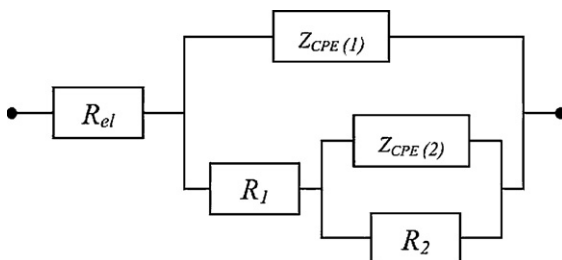

Fig. 6. Proposed equivalent circuit used to obtain impedance parameters.

Comparing the impedance parameters of P1 and P2 samples, it can be observed a reasonable similarity of capacitances $Z_{CPE(1)}$. On the other hand, P1 has a polarization resistance (R_1) of about 3 times lower than that corresponding to position P2. It seems that the corrosion protection consists of a cooperative action provided by both R_1 and R_2. Thus, the sample P2 has a better electrochemical corrosion behavior than that of sample P1. When these parameters are compared with those of the sample P3, it can be seen that the sum of R_1 and R_2 attains the highest value of all samples examined, which is associated with the best corrosion resistance. Besides, the highest R_2 value is also that of the sample P3, which can explain that trend to a slope of about 45° between 0.25 and 0.01 Hz, as shown in Fig. 4(c). Additionally, it is important to remark that the capacitance $Z_{CPE(1)}$ corresponds to the capacitance of double layer formation on the surface of the sample, and high $Z_{CPE(1)}$ indicates better electrochemical corrosion response.

3.2.3. Potentiodynamic polarization plots

Fig. 7 shows the potentiodynamic polarization curves obtained from −0.75 to −0.35 V (SCE) for the Pb–3.5 wt.% Sb alloy at three (03) different positions (P1, P2 and P3) corresponding to tests carried out in a stagnant and naturally aerated 0.5 M H_2SO_4 solution at 25 °C. Tafel extrapolation was used to obtain the experimental corrosion current density (i_{corr}) using both the cathodic and anodic branches of the polarization curves along a range of potentials from −450 to −550 mV (SCE). Parameters and observation of these results

Table 1
Impedance parameters of Pb–3.5 wt.% Sb alloy in 0.5 M H_2SO_4 solutions at room temperature.

Parameters	P1 $\lambda_1 = 30\,(\pm5)\,\mu m$ $\lambda_3 = NA$	P2 $\lambda_1 = 116\,(\pm13)\,\mu m$ $\lambda_3 = 33\,(\pm8)\,\mu m$	P3 $\lambda_1 = 160\,(\pm20)\,\mu m$ $\lambda_3 = 47\,(\pm6)\,\mu m$
R_{el} ($\Omega\,cm^2$)	4.4	5.1	4.1
$Z_{CPE(1)}$ ($\mu F\,cm^{-2}$)	411 (±2.5)	302 (±5)	802 (±41)
$Z_{CPE(2)}$ ($10^{-3} \times F\,cm^{-2}$)	2.9 (±0.2)	11.2 (±4)	0.05 (±0.01)
n_1	0.79	0.78	0.52
n_2	0.82	0.95	0.98
R_1 ($\Omega\,cm^2$)	118 (±4)	320 (±10)	73 (±6)
R_2 ($\Omega\,cm^2$)	215 (±21)	80 (±15)	803 (±35)
χ^2	93×10^{-4}	98×10^{-4}	33×10^{-4}

NA, not available.

reinforce the corrosion resistance tendency observed previously with the results of EIS and impedance parameters (equivalent circuit), i.e. better electrochemical corrosion resistance being associated with the sample P3.

Considering the Pb–3.5 wt.% Sb alloy at position P1, it is observed a current density of about 16 (±3) $\mu A\,cm^{-2}$ associated with a corrosion potential of about -521 mV (SCE). When similar parameters are observed for samples P2 and P3, the current densities and corrosion potentials are about 10 (±2) $\mu A\,cm^{-2}$ with -520 mV (SCE) and 5 (±2) $\mu A\,cm^{-2}$ with -493 mV (SCE), respectively. It is important to remark that there is no intention to describe the mechanism of dissolution and precipitation of the electrode system, which is widely discussed by Pavlov et al. [26,27].

3.3. Electrochemical behavior and resulting microstructures

It is known that during non-equilibrium solidification, the α-phase (Pb-rich) will have an increasingly Sb content from the dendrite arm center toward the interdendritic region up to the eutectic composition. The eutectic mixture is consisted by alternated Pb-rich and Sb-rich phases giving rise to galvanic cells formation.

It was recently reported [7,13] that a dendritic array has the antimony-rich regions located in the lamellar eutectic mixture. In this sense, it is believed that the Sb-rich lamellae envelope the Pb-rich phase more efficiently when a fine dendritic spacing is considered due to the more extensive distribution of the eutectic mixture, and thus protecting the Pb-rich matrix. Due to this reason, it is also believed that for Pb–Sb dendritic alloys with Sb content higher than 3 wt.%, a finer dendritic array would be more appropriate since it is associated with higher electrochemical corrosion resistance. This is the case of components which are manufactured by continuous casting processes.

Considering the samples examined in this present investigation, it was interesting to observe that with the increase in distance from the bottom of the casting, a trend to decrease the corrosion resistance is clearly confirmed. In order to better understand this apparently contradictory observation when compared with previous studies [7,13] with Pb–Sb alloys having dendritic arrays, the effects of the tertiary dendrite arm spacing associated with antimony macrosegregation for each sample (position) has been evaluated.

Fig. 8 depicts the percentage of interdendritic regions (black regions) compared with the Pb-rich matrix (white regions). In this
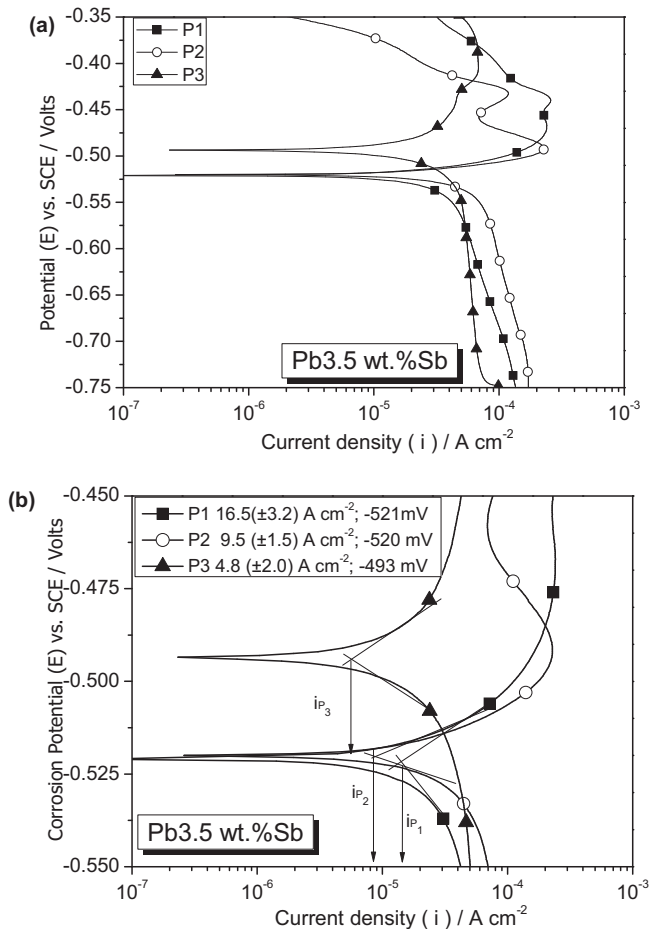

Fig. 7. Potentiodynamic polarization curves exhibiting current densities and corrosion potentials for Pb–3.5 wt.% Sb alloy samples in a 0.5 M H_2SO_4 solution at 25 °C: (a) from -0.75 to -0.35 V (SCE) and (b) from -0.55 to 0.45 V (SCE).
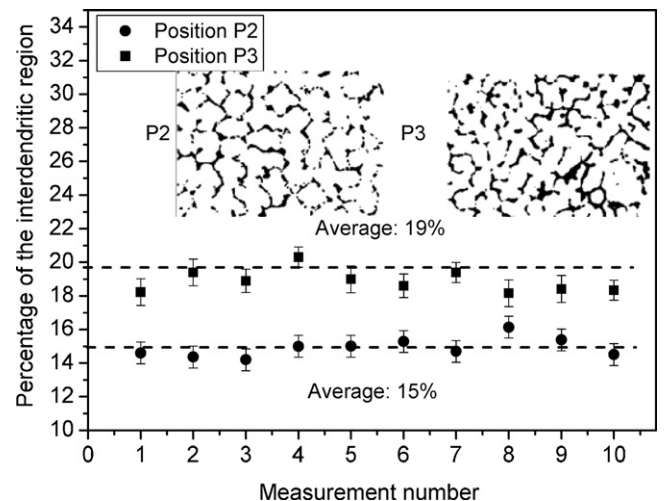

Fig. 8. Percentage of interdendritic region for positions P2 and P3 of the Pb–3.5 wt.% Sb alloy casting.

sense, two selected images of the resulting microstructures from positions P2 and P3 were converted to binary images and 10 measurements were carried out using the software ImageJ®. It can be seen that the position P3 has 19% of interdendritic region. This means that there exists a higher amount of tertiary arms (λ_3) in sample P3 than in P2, and this provides a more homogenous distribution of the eutectic mixture in the interdendritic region when compared with sample P2. Besides, a slightly higher amount of eutectic fraction is expected to occur at position (P3), due to the local higher Sb content caused by segregation, as previously depicted in Fig. 2(c).

These aforementioned assertions permit to explain the reason for which the sample P3 presented a better electrochemical corrosion response than the samples corresponding to the other two examined positions. Firstly, although the position P3 has both coarser primary and tertiary dendritic arms when compared with the corresponding values at P2, its resulting transverse microstructure array has a well defined network of tertiary arms permitting a more homogeneous distribution of the eutectic mixture between the dendritic arms and higher Sb content. This also helps to understand both the Bode and Bode-phase diagrams corresponding to this position, as previously discussed and evidenced in Fig. 4(a) and (b). Besides, it also helps to explain the displacement of about 30 mV (SCE) in the corrosion potential of sample P3 toward the nobler-side.

In this context, when the manufacturing of lead-acid battery components is considered, the evaluation of as-cast microstructures can be used as an alternative way to produce as-cast components with different corrosion resistance. In this sense, the choice of cooling rates which will be applied in the manufacturing process in order to attain the best electrochemical response of a Pb–Sb alloy casting should be associated with two initial operational parameters: (i) The antimony content of the alloy; and (ii) type of mould. These two parameters will be influent on the resulting cooling rate and microstructure which should be systematically investigated in order to permit the desired electrochemical corrosion response to be attained.

4. Conclusions

Based on the present experimental results concerning the microstructure dendritic array, macrosegregation solute profile and electrochemical behavior of a Pb–3.5 wt.% Sb alloy casting (i.e. impedance parameters, potentiodynamic polarization curves and equivalent circuit analysis), it can be concluded that the tertiary dendritic arm associated with the antimony segregation, which occurs during the casting process, have important roles on the resulting corrosion response. Samples of three transverse sections corresponding to different positions from the bottom of the casting (8, 25 and 50 mm) were examined. It was shown that the sample at position P1 (8 mm) has a dendritic array characterized by only primary (λ_1) and secondary dendrite arm spacings. When comparing

the resulting microstructural arrays of positions P3 and P2, it can be seen that the sample at position P3 has tertiary spacings (of about 50 μm) which are coarser than those observed at P2 (λ_3 of about 25 μm) but the continuity of the tertiary arms along the interdendritic region permits the eutectic mixture to be more homogeneously distributed. Considering that the antimony-rich region is located in the lamellar eutectic mixture, the Sb-rich lamellae envelope the Pb-rich phase contributing to the protection of the Pb-rich matrix against the corrosion. In this sense, it can also be concluded that the Sb content and the cooling rate during casting, which determines the magnitude of the dendritic array, are important parameters that should be considered in the manufacture of Pb–Sb alloys components with a view to improving their electrochemical corrosion behavior.

Acknowledgements

References

[1] R.D. Prengaman, J. Power Sources 67 (1997) 267–278.
[2] R.D. Prengaman, J. Power Sources 95 (2001) 224–233.
[3] R.D. Prengaman, in: K.R. Bullock, D. Pavlov (Eds.), Proceedings: Advances in Lead-Acid Batteries, vol. 84-14, The Electrochemical Society, Pennington, NJ, 1984, p. 201.
[4] R.D. Prengaman, J. Power Sources 158 (2006) 1110–1116.
[5] T. Hirasawa, K. Sasaki, M. Taguchi, H. Kaneko, J. Power Sources 85 (2000) 44–48.
[6] B. Rezaei, S. Damiri, J. Solid State Electrochem. 9 (2005) 590–594.
[7] W.R. Osório, D.M. Rosa, A. Garcia, J. Power Sources 175 (2008) 595–603.
[8] W.R. Osório, C. Aoki, A. Garcia, J. Power Sources 185 (2008) 1471–1477.
[9] L.C. Peixoto, W.R. Osório, A. Garcia, J. Power Sources 192 (2009) 724–729.
[10] W.R. Osório, L.C. Peixoto, A. Garcia, J. Power Sources 194 (2009) 1120–1127.
[11] W.R. Osório, L.C. Peixoto, A. Garcia, J. Power Sources 195 (2010) 1726–1730.
[12] L.C. Peixoto, W.R. Osório, A. Garcia, J. Power Sources 195 (2010) 621–630.
[13] W.R. Osório, D.M. Rosa, L.C. Peixoto, A. Garcia, J. Power Sources 196 (2011) 6567–6572.
[14] W.R. Osório, D.M. Rosa, A. Garcia, Electrochim. Acta 56 (2011) 8457–8462.
[15] W.R. Osório, D.M. Rosa, A. Garcia, Mater. Des. 34C (2012) 660–665.
[16] J. Campbell, Castings, 2nd ed., Butterworth-Heinemann, Oxford, Great Britain, 2003.
[17] K. Tsuj, P.J. Elving, Anal. Chem. 41 (1969) 216–218.
[18] F. Sá, O.L. Rocha, C.A. Siqueira, A. Garcia, Mater. Sci. Eng. A 373 (2004) 131–138.
[19] F. Mansfeld, M.W. Kendig, J. Electrochem. Soc. 135 (1998) 828–835.
[20] J. Pan, D. Thierry, C. Leygraf, Electrochim. Acta 41 (1996) 1143–1153.
[21] S. Gudic, J. Radosevic, M. Kliskic, Electrochim. Acta 47 (2002) 3009–3016.
[22] A. Cremasco, W.R. Osório, C.M.A. Freire, A. Garcia, R. Caram, Electrochim. Acta 53 (2008) 4867–4875.
[23] W.R. Osório, L.C. Peixoto, L.R. Garcia, A. Garcia, Mater. Corr. 60 (2009) 804–812.
[24] M. Aziz-Kerrzo, K.G. Conroy, A.M. Fenelon, S.T. Farrell, C.B. Breslin, Biomaterials 22 (2001) 1531–1539.
[25] W.R. Osório, A. Cremasco, P.N. Andrade, A. Garcia, R. Caram, Electrochim. Acta 55 (2010) 759–770.
[26] D. Pavlov, M. Bojinov, T. Laitinen, G. Sundholm, Electrochim. Acta 36 (1991) 2081–2086.
[27] D. Pavlov, M. Bojinov, T. Laitinen, G. Sundholm, Electrochim. Acta 36 (1991) 2087–2092.